Simulating the dynamic behavior of immiscible binary fluids in three-dimensional chemically patterned microchannels

Olga Kuksenok and Anna C. Balazs
Department of Chemical Engineering, University of Pittsburgh, Pittsburgh, Pennsylvania 15261, USA
(Received 6 January 2003; published 11 July 2003)

Using computer simulations, we investigate the behavior of an immiscible binary *AB* fluid that is driven to flow through a microchannel, which is decorated with a checkerboard pattern of chemically distinct *A*- and *B*-like patches on the top and bottom walls. We isolate conditions where the coupling between the imposed flow field and thermodynamic interactions yields a rich interfacial behavior between the *A* and *B* fluids and complex velocity patterns over the checkerboard domains. In effect, the *A* and *B* fluids undergo extensive mixing in specific regions of the channel, even for low Reynolds number flow. Decreasing the height-to-width ratio of the patterned microchannel enhances the extent of mixing between these two components. On the other hand, the length of the *A*/*B* interfaces is optimized in microchannels that have a square cross section. The results provide guidelines for designing microfluidic devices that can be used to effectively intermix multicomponent fluids.

DOI: 10.1103/PhysRevE.68.011502 PACS number(s): 64.75.+g, 47.11.+j

I. INTRODUCTION

In order to exploit the potential utility of microfluidic devices [1–3], it is critical to develop a fundamental understanding of the behavior of fluids flowing through micrometer-sized channels. Of particular interest is determining the behavior of immiscible binary fluids within these confined geometries. This is due in part to the potential for forming monodisperse oil-in-water and water-in-oil droplets or emulsions, which have applications in the pharmaceutical and food industries [4]. A more fundamental reason for the interest in confined immiscible fluids stems from the fact that, at these small dimensions, the interfacial tension between the liquids exerts a significant influence and can lead to behavior that is distinct from that in the bulk. Furthermore, fluid-wall interactions play a dominant role in the behavior of the confined liquids, and can be harnessed to control the flow patterns [5,6]. Numerous studies have shown that the phase behavior of binary mixtures is significantly affected by the wetting properties of the underlying surface [7–10]. It was also shown that the phase separation between the fluids can be controlled by using heterogeneous patterns on the substrate [11,12]; for thin films, the fluid is driven to mimic the design in the underlying surface [13]. One might expect that an external flow would significantly modify the surface-directed morphology. In terms of microfluidic applications, the use of a patterned substrate in an imposed flow field can offer an effective means of controlling the behavior of the mixture.

In previous studies [14,15], we used a computational model to examine the behavior in two dimensions of a binary fluid flowing over a patterned substrate within a microchannel. The binary fluid consisted of two immiscible components *A* and *B*, which were subjected to an imposed Poiseuille flow. The substrate was decorated with a checkerboard pattern of *A*- and *B*-like patches. The *A* fluid preferentially wet the *A* patches and the *B* fluid preferentially wet the *B* patches. Each component was driven to flow past the nonwettable domains to reach the wettable patches. As a consequence, the *A* and *B* fluids underwent extensive mixing within well-defined regions in the microchannels. Recall that the Reynolds number in such micrometer-sized channels is sufficiently low that the fluids exhibit laminar flow, which limits the degree of mixing between components [3]. As a result, vital reagents and samples cannot undergo extensive interactions. In order to carry out a broad range of chemical reactions within microfluidic devices, it is highly important to develop simple schemes that promote the mixing of multicomponent fluids within microchannels [16].

Two-dimensional (2D) studies are appropriate in cases where the height-to-width ratio in the channel is relatively low. In this paper, we expand our computational studies of binary fluids in chemically patterned microchannels to three dimensions. We again focus on the flow and phase behavior of immiscible fluids *A* and *B* that are driven by an imposed pressure gradient through the microchannel. In the 3D simulation, both the top and bottom walls of the channel are decorated with a checkerboard pattern of *A* and *B* patches, as shown in Fig. 1. Our results indicate that the flow behavior in a rectangular channel, which has a low height-to-width ratio, is similar to the behavior in the 2D simulations; however, the behavior in a 3D channel that has a square cross section is

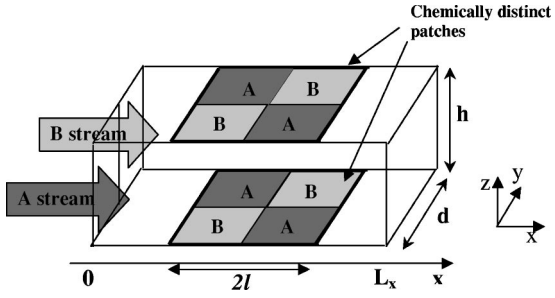

FIG. 1. Schematic of system. The top and bottom substrates are decorated with a checkerboard pattern of *A*-like and *B*-like patches. The system exhibits two-stream flow at the beginning of the channel ($x=0$).

fundamentally different and is characterized by the formation of complex interfaces between the two fluids.

Below, we first detail the geometry of the patterned microchannel and describe the equations that characterize our system. We then discuss how the interfacial behavior and degree of mixing within this chamber depends on the system parameters.

II. THE MODEL

We consider the microchannel shown in Fig. 1. Both the top and bottom of this channel are decorated with a checkerboard pattern of *A* and *B* patches; the checkerboard on the top is in registry with the one on the bottom. In our simulations, the entire channel is $100\times40\times40$ lattice sites in size and the length of the each patch is 30 lattice sites.

An imposed pressure gradient (Poiseuille flow) drives two immiscible fluids *A* and *B* to move past the patches and on through the channel. The first *A*-like patch is placed in the path of the *B* fluid and the first *B*-like patch lies in the path of the *A* stream. Since the *A* (*B*) fluid preferentially wets the *A* (*B*) regions, the first set of patches distorts the initial distribution of the liquids. The arrangement of patches is reversed in the next row, driving these liquids back to their original distribution. As we show below, the routing of the *A* and *B* components though the channel is significantly affected by the patches and leads to the creation of new interfaces between these species.

To characterize the morphology of the fluid, we define an order parameter $\varphi(r,t)=\rho_A(r,t)-\rho_B(r,t)$ where $\rho_i(r,t)$ represents the local number density of the ith component, $i=A,B$. The thermodynamic behavior of the system is described by the free energy functional $F=F_0+\Psi_S$, where F_0 is the Ginzburg-Landau free energy for a binary mixture [17]

$$F_0=\int d\vec{r}\left[-\frac{a}{2}\varphi^2+\frac{b}{4}\varphi^4+\frac{k}{2}|\vec{\nabla}\varphi|^2\right]. \tag{1}$$

We consider the fluid to be in the two-phase coexistence regime, where the equilibrium order parameter for the *A* (*B*) phase is $\varphi_{A(B)}=\pm\varphi_{eq}$, $\varphi_{eq}=\sqrt{a/b}$. The term $(k/2)|\vec{\nabla}\varphi|^2$ represents the free energy of forming interfaces between the *A* and *B* fluids. The second term in the free energy functional, Ψ_S, is a potential that describes the interaction between a fluid element at the point $\vec{r}$ and the patterned substrate. Specifically, we take [18]

$$\Psi_s=\int d\vec{r}\int d\vec{s}\left(\frac{1}{2}Ve^{-|\vec{r}-\vec{s}|/r_0}[\varphi(\vec{r})-\tilde{\varphi}(\vec{s})]^2\right), \tag{2}$$

where the inner integral represents integration over the substrates. The constant V characterizes the strength of the interaction, and r_0 represents the range of this interaction. Note that $V=0$ outside the patterned regions. We choose $\tilde{\varphi}(\vec{s})=\varphi_{A(B)}$ to introduce the respective *A*- and *B*-wetted regions at specific regions on the substrate. Thus, the free energy F is reduced when the fluid is *A*-rich near *A*-like patches and the fluid is *B*-rich near the *B*-like patches [19].

The evolution of order parameter for this system is described by the Cahn-Hillard equation, in which the flux of φ is proportional to the gradient of the chemical potential μ and is given by [17,21]

$$\frac{\partial\varphi}{\partial t}+\vec{v}\cdot\vec{\nabla}\varphi=M\nabla^2\mu, \tag{3}$$

where $\mu=\delta F/\delta\varphi$ and M is the mobility of the order parameter.

The velocity field $\vec{v}$ obeys the Navier-Stokes equation in the overdamped limit (this limit is appropriate for low-Reynolds-number flow) [17,21]:

$$\vec{0}=-\vec{\nabla}p-\vec{\nabla}P+\eta\nabla^2\vec{v}+\frac{\delta F}{\delta\varphi}\vec{\nabla}\varphi. \tag{4}$$

Here, η is the shear viscosity of the fluid, $\vec{\nabla}P$ represents the imposed pressure gradient along the channel, and p is a Lagrange multiplier that guarantees the incompressibility condition $\vec{\nabla}\cdot\vec{v}=0$. The term $(\delta F/\delta\varphi)\vec{\nabla}\varphi$ represents a thermodynamic force that drives the system toward thermodynamic equilibrium.

In order to rewrite Eqs. (3) and (4) in dimensionless units, we choose a characteristic length scale ζ and a time scale $\tau=\zeta^2/aM$, which is equal to the diffusion time through the distance ζ. The order parameter value is normalized by φ_{eq}. It should be noted that normally in investigations of phase separation in infinite volumes, the most appropriate choice for the characteristic length is the thickness of the interface, $\zeta_{int}=\sqrt{k/a}$ [21]. Here, however, we will ultimately consider fluids with different interfacial properties and thus we maintain ζ_{int} as an independent variable. Nevertheless, our choice for the characteristic length scale can be rewritten in terms of the interface length as $\zeta=\zeta_{int}/\sqrt{\tilde{k}}$, where we have defined the dimensionless parameter $\tilde{k}$ as $\tilde{k}=k/(a\zeta^2)$. The interfacial tension can be defined as $\sigma\approx k\varphi_{eq}^2/\zeta_{int}=\varphi_{eq}^2 a\zeta\sqrt{\tilde{k}}$.

Equations (3) and (4) can now be rewritten in the dimensionless units

$$\frac{\partial\varphi}{\partial t}+\vec{v}\cdot\vec{\nabla}\varphi=\nabla^2\mu, \tag{5}$$

$$\vec{0}=-\vec{\nabla}p+\nabla^2\vec{v}+C\frac{\delta F}{\delta\varphi}\vec{\nabla}\varphi+\vec{H}, \tag{6}$$

where $\vec{H}=-\vec{\nabla}P\tau\zeta/\eta$ is the dimensionless form of the imposed pressure gradient $\vec{\nabla}P$, and the constant $C=\sigma\zeta/a\eta M\sqrt{\tilde{k}}$ defines the ratio between the viscous force and interfacial tension, and therefore plays the role of the capillary number [21]. Because the pressure gradient is applied along the x axis, only the x component of the vector $\vec{H}$ is nonzero, $H_x\equiv H$.

We impose the following boundary conditions for Eq. (5) at the walls of the channel: $(\partial\mu/\partial n)|_{wall}=0$, $[\partial\varphi(\vec{s})/\partial z]|_{z=0,h}=k^{-1}\int d\vec{s}_i\{V(\vec{s}_i)[\varphi(\vec{r})-\tilde{\varphi}(\vec{s}_i)]\}|_{\vec{r}\to\vec{s}}$, and $(\partial\varphi/\partial y)|_{y=0,h}=0$. At the entry of the channel, we have two-

stream flow; at the exit, we assume free draining flow, i.e., $(\partial\varphi/\partial x)|_{x=L}=0$. We have no-slip boundary conditions for the velocity at the walls, and we assume an undistorted Poiseuille profile at the beginning and at the end of the channel.

We use a cell dynamic system (CDS) method [22] to update the value of φ in Eq. (5). By employing CDS modeling (rather than a conventional discretization of the equation), we can significantly increase the computational speed of the simulation. The velocity field in the system is a superposition of the Poiseuille profile $\vec{v}_{Pois}$ and the velocity field $\vec{u}$, which describes the distortion of Poiseuille profile; thus, $\vec{v}=\vec{v}_{Pois}+\vec{u}$. Given that $\vec{0}=\nabla^2\vec{v}_{Pois}+\vec{H}$, Eq. (6) can be rewritten for the velocity $\vec{u}$ as

$$\vec{0}=-\vec{\nabla}p+\nabla^2\vec{u}+C\frac{\delta F}{\delta\varphi}\vec{\nabla}\varphi. \tag{7}$$

This equation, coupled with the incompressibility equation $\vec{\nabla}\cdot\vec{u}=0$ and the condition that $\vec{u}=\vec{0}$ at all the boundaries, can be solved by the spectral τ method [23]. The components of the velocity $\vec{u}$ and the pressure p are assumed to be in the form of truncated series:

$$u_i=\sum_{n=0}^{N}\sum_{m=0}^{M}\sum_{l=0}^{L}U^i_{nml}\psi_{nml}, \tag{8}$$

$$p=\sum_{n=0}^{N}\sum_{m=0}^{M}\sum_{l=0}^{L}P_{nml}\psi_{nml}, \tag{9}$$

where $i=x,y,z$ denotes the ith component of the velocity and U^i_{nml} and P_{nml} are unknown coefficients. The ψ_{nml} are elements of the complete set of orthogonal functions, $\psi_{nml}=T_n(2x/L_x-1)T_m(2y/d-1)T_l(2z/h-1)$, where $T_n(x)=\cos(n\arccos x)$ are the Chebyshev polynomials. The important feature of the spectral τ method [23] is that the functions ψ_{nml} are not individually required to satisfy the boundary conditions. All necessary boundary conditions are imposed through additional constraints on the unknown coefficients [24]. In all simulations presented below, the solution converges relatively rapidly with increases in N, M, and L. Here, we set $N=16$, $M=8$, and $L=8$; further increases in these values led to negligibly small ($<1\%$) changes in all integrated values that we used to characterize our system.

III. RESULTS AND DISCUSSION

In the first study, we consider the flow patterns in the microchannel for different values of the imposed pressure gradient (i.e., imposed velocities). In order to describe changes in the system as we vary H, we define λ as the characteristic length along the x axis over which the order parameter distribution is significantly distorted from the thermodynamically determined configuration. This length is proportional to the velocity in the center of channel, v_{max}. We define δ as the characteristic length along the z axis over which thermodynamics dominates and the A (B) fluid is localized near the A (B) patches. This length is determined by

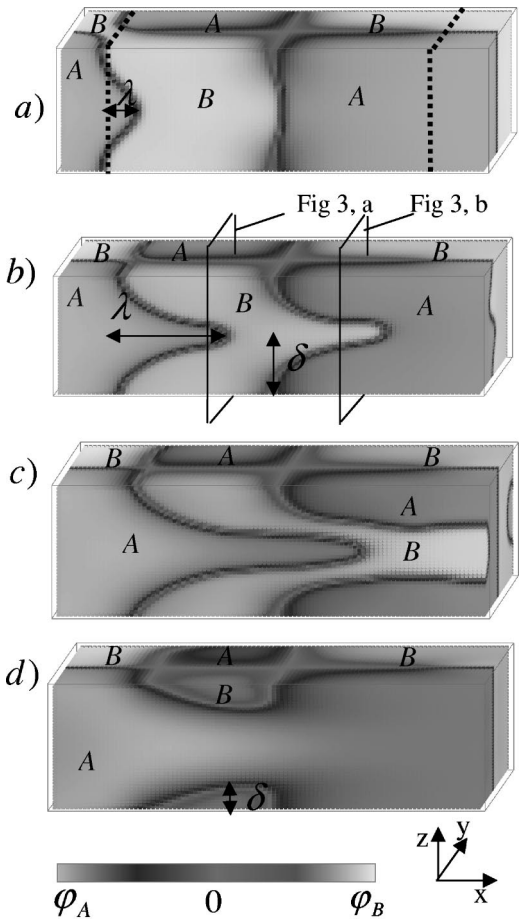

FIG. 2. Order parameter distribution at steady state for different values of H: (a) $H=10^{-5}$, (b) $H=10^{-4}$, (c) $H=3\times10^{-4}$, and (d) $H=10^{-3}$. The remaining parameters that characterize the system are $l=30$, $h=40$, $d=40$, $L_x=100$, $r_0=5$, $V=0.003$, $C=50$, and $t=20\,000$ time steps. The lightest gray domains represent the B fluid, the darker gray areas indicate the A fluid, and the darkest gray regions mark the intermediate values of the order parameter.

a competition between the interfacial tension and imposed velocity; higher values of interfacial tension lead to a larger δ (where higher velocities are needed to break up the interface). Due to the complicated interfacial behavior and flow patterns in the system, the specific values of both λ and δ cannot be readily predicted analytically; they can, however, be estimated from the simulations and provide a useful means of characterizing the changes in the system with changes in H.

For low velocities, the fluid mimics the structure of underlying pattern, as can be seen in Fig. 2(a). This configuration corresponds to the minimum of the free energy, $F=F_0+\Psi_S$. The low-velocity regime is observed when the advective term in Eq. (5) is much smaller than the diffusive term. For this case, distortions in the thermodynamically determined distribution of φ, which are caused by the imposed flow, are significant only at the beginning of the patterned region and in the region between the first and second sets of patches. In the low-velocity regime, λ is smaller then l, the length of a patch. It should be noted that the case where the patch length goes to infinity corresponds to the low-velocity

regime for any finite value of imposed velocity. In this case, even if λ is large, it is always smaller than l; thus, the fluid always mimics the pattern at the end of each set of patches.

Increases in the imposed pressure gradient led to more significant changes in the order parameter distribution [see Figs. 2(b) and 2(c)]. We will refer to this regime as the intermediate-velocity regime and we will return to a detailed description of this regime below. Further increases in H lead to the last of the possible regimes, the high-velocity regime, where flow through the channel does not exhibit significant distortions in the middle of the channel, while near the top and the bottom of the substrates, the order parameter distribution is determined by wetting properties of the patches [see Fig. 2(d)]. The other limiting case of the patch design, where the patch length l goes to zero, effectively corresponds to the high-velocity regime even for low velocities. (If the patch length equals zero, the two fluid streams remain undistorted and flow parallel to each other along the channel.)

The intermediate-velocity regime [Figs. 2(b) and 2(c)] shows the most interesting and complicated structure inside the region that encompasses the patterned substrates. Both λ and δ are close to their limiting values, which are determined by the geometry of the channel; namely, in the case shown in Fig. 2(b), λ is slightly smaller than the length of the patch l, and δ has its maximum value, $\delta \approx h/2$. On the other hand, in the Fig. 2(c), the value of δ is slightly lower than its limiting value. However, the value of λ exceeds the length of the patch l. Thus, Figs. 2(b) and 2(c) represent limiting cases of the intermediate-velocity regime.

Further insights into the features of the intermediate-velocity regime can be obtained by viewing cross sections that lie perpendicular to the flow direction. Figures 3(a) and 3(b) show examples of the flow patterns and morphology in the planes that are marked in Fig. 2(b). The black arrows indicate the direction of the fluid flow and the size of the arrows indicates the magnitude of the velocity. We can see rich interfacial behavior and complex velocity patterns in the middle of the channel, while the morphology near the substrates is determined by the preferential wetting interactions.

The cases shown in Fig. 2 correspond to the steady-state regime inside the patterned region [25]. In order to better understand the complex steady-state behavior, we examine the evolution of the system for all these cases. For the specific example where $H=3\times10^{-4}$, Fig. 4 shows the behavior of the system at relatively early times, when the A (B) patches in the first box of the patterned region are already covered by the A (B) fluid. As the A stream initially flows past the first energetically unfavorable B-like region, thermodynamic interactions drive the A fluid to diffuse toward the adjacent A-patch. In addition, the fluid moves to the center of the channel by advection. Figure 4(a) shows an example of the morphology and velocity profile in a vertical cross section through the channel. The arrows (which represent the velocity field) appear to be largest near the center of each patch along the z direction, indicating the vertical flow of the fluid away from the unfavorable domains. By examining a horizontal cross section through the channel [Fig. 4(b)], we can see that in the layers close to the substrate there is significant distortion of the parabolic Poiseuille velocity profile.

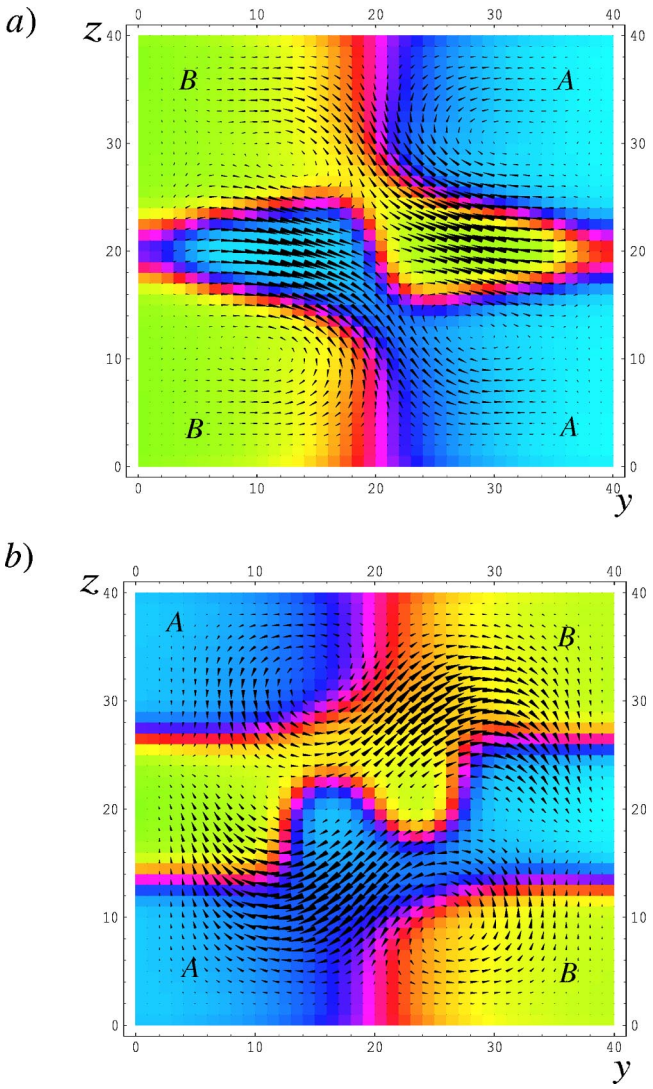

FIG. 3. Order parameter distributions and velocity fields at the vertical cross sections marked in Fig. 2(b). In (a) $x=40$ and in (b) $x=60$. The arrows indicate the velocity field and the size of the arrows is proportional to the absolute value of the velocity.

In particular, a close look at the arrows in the central region shows the appearance of a y component in the velocity profile.

Figures 4(c) and 4(d) show the actual values of u_x and u_z, respectively, near the horizontal cross section in Fig. 4(b). In the absence of the patches, the plot in Fig. 4(c) would have a simple parabolic shape; here, however, the peak values of u_x are higher than the corresponding undistorted values because of the fluid streams that come from the top and bottom surfaces to the center of channel. To understand the image in Fig. 4(d), recall that in the absence of the patches, the system would exhibit undistorted Poiseuille flow, where u_z is zero (and thus the plot would be a flat plane). The appearance of the peaks in Fig. 4(d) reflects the enhanced vertical flow of the fluids [as seen in Fig. 4(a)] due to the presence of the patches [26].

To quantify the behavior of the fluid, and in particular the effective mixing in the system, we define the following two

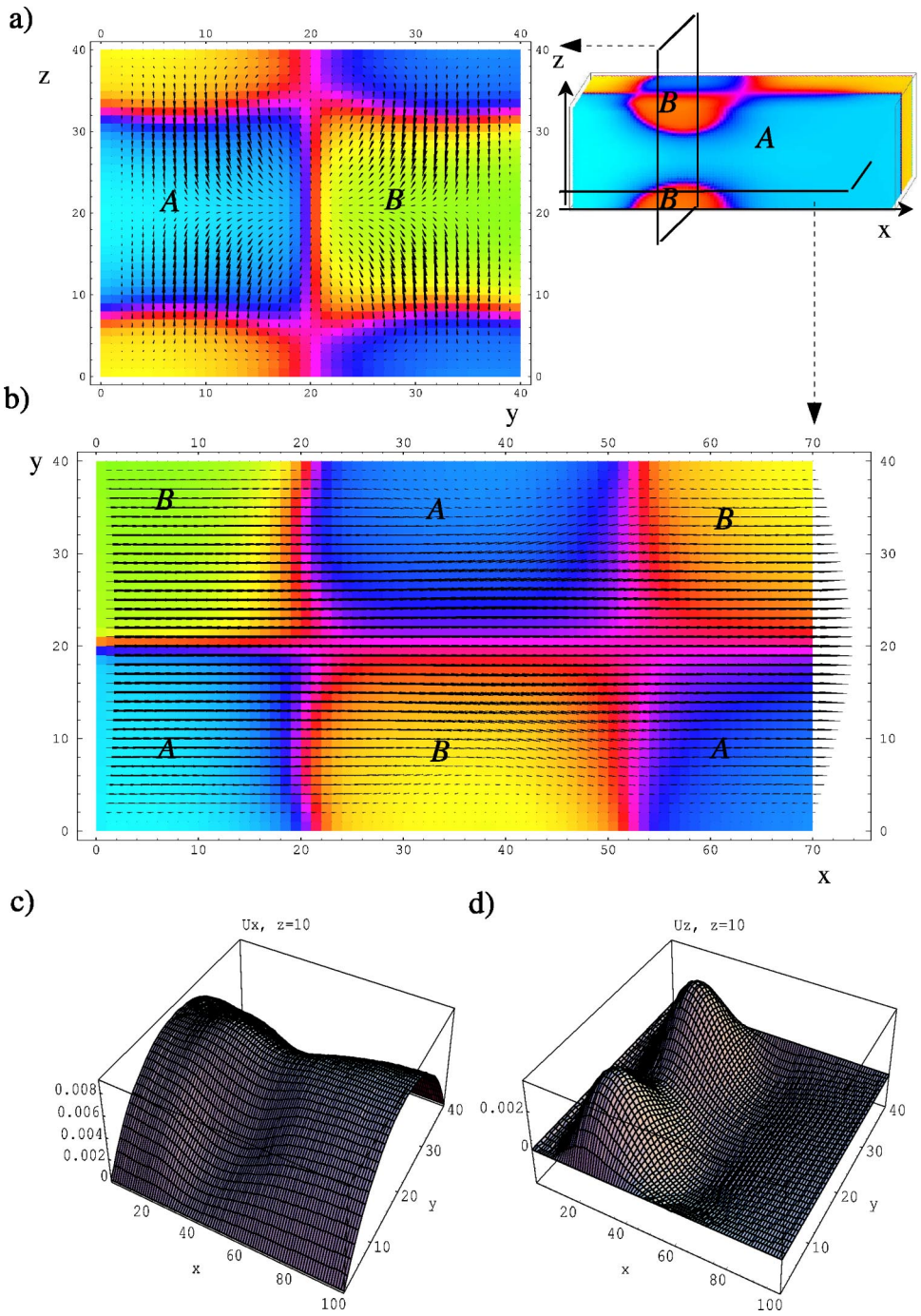

FIG. 4. (a) Order parameter distribution and velocity field at the vertical cross section (in the yz plane) at $x=25$ in the channel. (b) Order parameter distribution and velocity field at the horizontal corss section at $z=6$ in the channel. (c) Value of the x component of the velocity in the horizontal cross section at $z=10$. (d) Value of the z component of the velocity in the horizontal cross section at $z=10$. All system parameters are the same as in Fig. 2(c), but here the system is at an early time, $t=5000$ time steps.

parameters. Specifically, to calculate the extent of mixing inside the volume V that encompasses the patterned substrates, we define $M(t)$ as the volume where the order parameter value is lower than some characteristic value. Specifically, we sum over the points i where $\varphi<0.25\varphi_{eq}$, so that $M(t)=(1/V)\Sigma i$. We also calculate (by the broken-bond method [27]) the area of the interface between the A and B fluids and normalize this quantity by the volume V; we refer to this parameter as I.

Figures 5 and 6 show the evolution of I and M, respectively, for different values of the imposed pressure gradient, H. (The morphologies at steady state for the same values of H are shown in the Fig. 2.) For early times, curves for I at different values of H lie on one line; the same is observed for the early-time plots of M. The reason for this behavior is that the main process in the system at the early times is the diffusion of the fluid to the appropriate patches. At the beginning of the simulations ($t=0$), the initial conditions impose undistorted two-stream flow, but the cost in free energy for having each component near the nonwettable patches is sufficiently high that the fluids diffuse toward the wettable domains until the A (B) patches are covered by the A (B) fluid, where the thickness of the fluid layer is at least equal to r_0. The corresponding characteristic time can be estimated as $\tau_1 \sim r_0^2/V_{eff}$, where V_{eff} represents the strength of interaction, averaged over the fluid layer of thickness r_0. For the

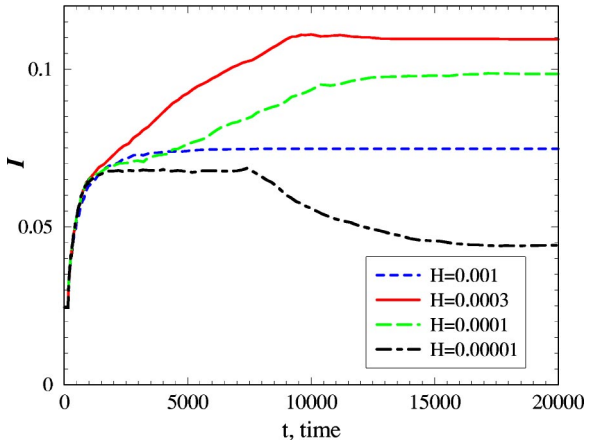

FIG. 5. Interface area I for cases (a)–(d) in Fig. 2.

simulation values corresponding to the Figs. 5 and 6, $\tau_1 \approx 1000$ time steps.

When the A (B) patterns are covered by the A (B) fluid layer, a competition between thermodynamic interactions and advection gives rise to complicated flow patterns and morphology in the channel. The time that is needed for the system to reach steady state is shortest for the highest imposed velocity, $\tau \sim l/v_{max}$, where v_{max} is the value of the velocity in the middle of the channel. For low values of imposed velocities, where thermodynamics plays a dominant role, the late-time behavior is determined by the phase separation process, which leads to a decrease in both the interface length and mixing area (dot-dashed curves in Figs. 5 and 6).

The richest interfacial behavior is observed for the case of intermediate values of H (curves drawn with a solid line and long dashes in Fig. 5). The length of the interface increases almost by a factor of 5 relative to the case without the checkerboard pattern. In the region of H where we observe this behavior, we find that the values of the characteristic lengths are $\lambda \approx l$ and $\delta \approx h/2$ [see Figs. 2(b) and 2(c)].

On the other hand, the largest area of mixing corresponds to the highest value of H (dashed curve in Fig. 6). We find that relatively high velocities lead to a widening of the A (B) interfaces inside the channel. The wider interfaces lead to greater areas of mixing.

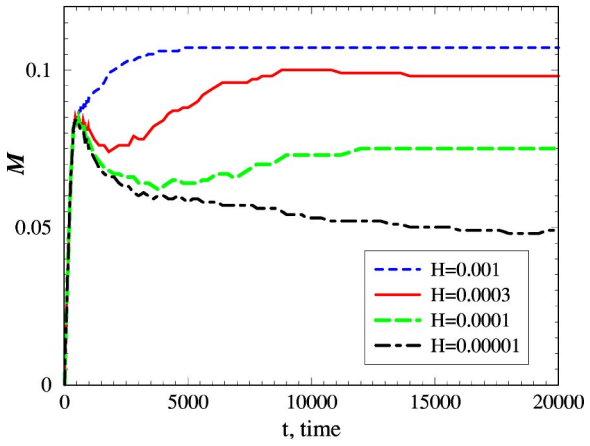

FIG. 6. Mixing area M for cases (a)–(d) in Fig. 2.

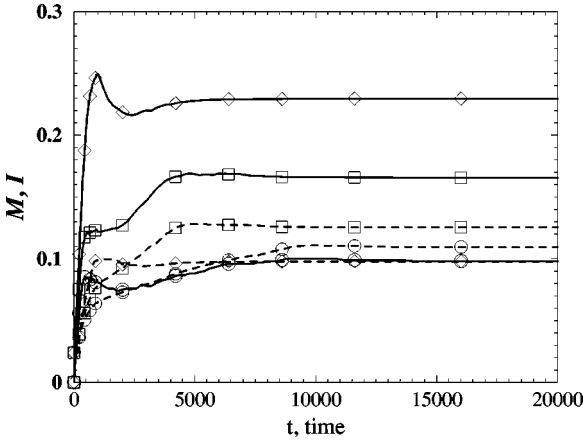

FIG. 7. Time evolution of the interface area I (dashed curves) and mixing area M (solid curves) for different values of the channel height. The plot for $h=20$ is marked with diamonds, the graph for $h=30$ is marked by squares, and the curve for $h=40$ is marked with circles. All other parameters are the same as in Fig. 2(c).

Despite the complex morphology and flow patterns, the mixing inside the channel is not extensive; the volume where the fluids are actually mixed occupies only about 10% of the volume inside the patterned region. In the next study, we analyzed the fluid behavior in rectangular channels. We decreased the height-to-width ratio and applied the appropriate value of H to maintain the same imposed Poiseuille velocity in the center of the channel for all channel heights.

The solid lines in Fig. 7 show the time evolution of M for the different channel heights. We can see that the mixing area strongly increases with the decreases in the height-to-width ratio, and reaches 25% for a rectangular channel with a height that is half of the width (solid line with diamonds in Fig. 7). On the other hand, the difference in the steady-state values of I is not that significant. The reason for this behavior is the following. The limiting value of δ is equal to $h/2$ and therefore this value decreases with decreasing channel height. Thus, even if we keep all the other system parameters the same, we effectively switch the system to the low-velocity regime as we defined it above, and that is why I is smallest for the smallest channel height (dashed curve with diamonds, Fig. 7). But the absolute value of the velocity is relatively high; as we noted above, large H leads to very wide A (B) interfaces, or mixing areas, inside the channel.

Further decreases in the height-to-width ratio become too computationally intensive because, to accurately discretize such small systems, one would have to rescale the lattice size and therefore increase both the length and the width of the channel. On the other hand, this system becomes effectively two dimensional and it is reasonable to use 2D modeling, for example, as was done in [14,15].

Finally, we note that we can equate our simulation parameters with typical experimental values through the following arguments. If we take experimentally relevant values for the viscosity of the fluid η, the diffusion constant aM, and the interfacial tension σ, and recall that in these studies we set $C=50$, we can relate the length scale in our simulation ζ (a lattice spacing), to a physical length scale through the fol-

lowing equation: $\zeta = 0.7CaM\eta/\sigma$. From this value for the lattice spacing, we can specify the height and the width of the channel. As we noted in Sec. II, we can then calculate a time step as $\tau = \zeta^2/aM$ and therefore the velocity in the middle of the channel, v_{max}. In addition, if we assume a value of ρ, we can calculate the Reynolds number for our system, $\mathrm{Re} = \rho v_{max} h/\eta$.

IV. CONCLUSIONS

In the above simulations, we examined the behavior of binary immiscible fluids driven by an imposed pressure gradient through a 3D microchannel that is decorated with chemically distinct patterns on the top and bottom substrates of the channel. We examined the effects of varying the imposed velocity, from relatively low to high values of this parameter on the interfacial area *I* and extent of mixing *M* between the two fluids. The most striking behavior was observed in the intermediate velocity regime, where a coupling between thermodynamic interactions and the imposed flow field gives rise to rich interfacial behavior between the *A* and *B* fluids and complex velocity patterns over the checkerboard domains. In this intermediate region, new *A*/*B* interfaces lead to effective increases in the interface area. The extent of mixing, however, is greatest in the high-velocity regime, where the enhanced flow increases the width of the interfaces.

We found that in the case of a channel with a square cross section the volume in which the fluids were extensively mixed occupied about 10% of the volume of the region that encompasses the patterned substrates. Decreasing the height-to-width ratio, however, leads to increases in the value of *M*, yielding values up to 25% for a channel that has a height-to-width ratio of 0.5. The interface length does not change significantly with variations in the channel height, because the free energy cost of forming a large interfacial area in channels with low height-to-width ratio is too large. Therefore, relatively wide mixing regions can be created by introducing chemically patterned substrates in microchannels with a low height-to-width ratio, while the effect of creating additional interfaces dominates in channels with a square cross section.

ACKNOWLEDGMENTS

The authors acknowledge helpful discussions with Professor Julia Yeomans, Professor David Jasnow, and Rene Hurka. A.C.B gratefully acknowledges financial support from ONR.

[1] D.R. Reyes, D. Iosifidis, A. Manz, Anal. Chem. **74**, 2623 (2002).
[2] Deirdre R. Meldrum and Mark R. Hall, Science **297**, 1197 (2002).
[3] G.M. Whitesides and A.D. Stroock, Phys. Today **54**(6), 42 (2001).
[4] P.B. Umbanhowar, V. Prasad, and D.A. Weitz, Langmuir **16**, 347 (2000), and references therein.
[5] B. Zhao, J. Moore, and D.J. Beebe, Science **291**, 1023 (2001).
[6] D.E. Kataoka and S. Troian, Nature (London) **402**, 794 (1999).
[7] S. Puri and S.L. Frisch, J. Phys.: Condens. Matter **9**, 2109 (1997).
[8] S. Puri and K. Binder, Phys. Rev. A **46**, R4487 (1992); Phys. Rev. E **49**, 5359 (1994).
[9] H. Tanaka, Phys. Rev. Lett. **70**, 53 (1993); **70**, 2770 (1993).
[10] S. Dietrich, J. Phys.: Condens. Matter **8**, 9127 (1996).
[11] A. Karim *et al.*, Phys. Rev. E **57**, R6273 (1998).
[12] C. Bauer and S. Dietrich, Phys. Rev. E **60**, 6919 (1999).
[13] M.K. Chaudhury and G.M. Whitesides, Science **256**, 1539 (1992).
[14] O. Kuksenok, J.M. Yeomans, and A. Balazs, Langmuir **17**, 7186 (2001).
[15] O. Kuksenok, J.M. Yeomans, and A. Balazs, Phys. Rev. E **65**, 031502 (2002).
[16] A.D. Stroock *et al.*, Science **295**, 647 (2002).
[17] A.J. Bray, Adv. Phys. **43**, 357 (1994).
[18] A.C. Balazs *et al.*, J. Phys. Chem. B **104**, 3411 (2000).
[19] Other possible choices for the fluid-substrate interaction involve a short-range interaction that is introduced only through the appropriate boundary condition (for example, as in [8]), or long-range interactions due to van der Waals forces or double layer forces [20]. One can also assume a long-ranged Lennard-Jones type of interaction between the fluid and substrate elements (for example, as in Ref. [12]). For small dimensions, for example if the channel height is 1 μm or lower, even a short-ranged interaction already extends significantly into the bulk. In Eq. (2), we chose the simplest form of the interaction potential. This potential basically implies a preferential value of the order parameter on the substrate and decays away from the substrate as a function of distance. It therefore gives a reasonable phenomenological description without specifying the exact type of interaction or atomic structure of the substrate. We note that using a power law decay instead of an exponential decay in Eq. (2) does not change the results qualitatively, if one chooses parameters to maintain the same effective strength and range of interaction.
[20] P.G. de Gennes, Rev. Mod. Phys. **57**, 827 (1985).
[21] D. Jasnow and J. Vinals, Phys. Fluids **8**, 660 (1996).
[22] Y. Oono and S. Puri, Phys. Rev. A **38**, 434 (1988).
[23] D. Gottlieb and S. Orszag, *Numerical Analysis of Spectral Methods: Theory and Applications* (Arrowsmith, Bristol, 1977).
[24] Substitution of Eqs. (8) and (9) into Eq. (7), together with the incompressibility condition, yields a system of $4(N+1)(M+1)(L+1)$ equations for $4(N+1)(M+1)(L+1)$ unknown coefficients U^i_{nml} and P_{nml}. In the τ method, *n* of these equations are replaced by *n* additional constraints, which allows us to impose $u_i = 0$ at the boundaries. (The name ''tau method'' originates from the fact that the resulting approximation [Eq. (8)] is the exact solution to a modified problem, which differs from the original one by a small (tau) term [23]).
[25] We also find that in a narrow range of the imposed pressure

gradient (corresponding to a transition between the intermediate- and high-velocity regimes), the system's characteristics can exhibit nondecaying periodic oscillations, which correspond to periodic droplet formation on the sidewalls. This morphological instability occurs even in the absence of hydrodynamic interactions. The range of H where we observed this behavior is narrow and is approximately 0.4% of the interval we consider, for example, in Fig. 2 (H varies from 10^{-5} to 10^{-3}). In the present paper, we study the general behavior of the system; the investigation of the regime where the instability and droplet formation occur is the subject of a separate study [O. Kusenok, D. Jasnow, J. Yeomans, and A. Balazs (unpublished)].

[26] These peaks are higher for higher values of C; in fact, all distortions of the original Poiseuille velocity profile increase with increases in C. (Nonetheless, we observed that the overall behavior of the system is qualitatively similar for the higher values of C studied here.)

[27] T. Ohta, D. Jasnow, and K. Kawasaki, Phys. Rev. Lett. **49**, 1223 (1982).